Porous Zr2SC-carbon composite microspheres: Possible radiation tolerant sorbents and transmutation hosts for technetium-99

Nicholas Scales
ANSTO, ns112@uowmail.edu.au

Jun Chen
University of Wollongong, junc@uow.edu.au

Robert Aughterson
ANSTO

Inna Karatchevtseva
ANSTO

Attila Stopic
ANSTO

See next page for additional authors

Follow this and additional works at: https://ro.uow.edu.au/aiimpapers

Part of the Engineering Commons, and the Physical Sciences and Mathematics Commons

Porous Zr2SC-carbon composite microspheres: Possible radiation tolerant sorbents and transmutation hosts for technetium-99

Abstract

The preparation, characteristics and adsorption properties of novel porous carbon-ceramic composite microspheres are presented. The composites were synthesised by a simple ion exchange process involving the cationic Zr tetramer and commonly-available macroporous sulphonated polystyrene-divinylbenzene cation exchange resins, with subsequent carbothermal reduction at 1350 °C. The materials were extensively characterised with respect to composition, chemical structure and porosity. Carbothermal reduction of the Zr-loaded templates resulted in formation of crystallites of the MAX phase zirconium sulphide carbide (Zr_2SC) embedded within a highly microporous carbon framework with a macroporous secondary structure inherited from the resin template. Despite the high BET surface areas of the Zr_2SC-carbon composite microspheres (in some cases, greater than 600 $m^2 g^{-1}$), they are extremely mechanically robust. The microspheres displayed high adsorption selectivity for oxoanions relative to cationic solution species, including perrhenate (ReO_4^-), a pertechnetate (TcO_4^-) surrogate. Accumulation of ReO_4^- on the Zr_2SC particles was unequivocally demonstrated by elemental mapping. Such materials are potential candidates as combined ^{99}Tc sorbents and reusable transmutation hosts.

Disciplines

Engineering | Physical Sciences and Mathematics

Authors

Nicholas Scales, Jun Chen, Robert Aughterson, Inna Karatchevtseva, Attila Stopic, Gregory R. Lumpkin, and Vittorio Luca

1 **Porous Zr₂SC-carbon composite microspheres: possible radiation**

2 **tolerant sorbents and transmutation hosts for technetium-99**

3 Nicholas Scales[a, *], Jun Chen[b], Robert D. Aughterson[a], Inna Karatchevtseva[a], Attila Stopic[a],

4 Gregory R. Lumpkin[a] and Vittorio Luca[c, *]

5 [a]Australian Nuclear Science and Technology Organisation, Locked Bag 2001, Kirrawee

6 DC, New South Wales, 2232, Australia

7 [b]Intelligent Polymer Research Institute, ARC Centre of Excellence for Electromaterials

8 Science, Australian Institute of Innovative Materials, University of Wollongong, Innovation

9 Campus, North Wollongong, NSW 2522, Australia

10 [c]Programa Nacional de Gestión de Residuos Radiactivos, Comisión Nacional de Energía

11 Atómica, Centro Atómico Constituyentes, Av. General, Paz 1499, 1650 San Martin,

12 Provincia de Buenos Aires, República Argentina

13 [*]Corresponding authors (nsz@ansto.gov.au; vluca@cnea.gov.ar)

14

15 **Abstract**

16 The preparation, characteristics and adsorption properties of novel porous carbon-ceramic

17 composite microspheres are presented. The composites were synthesised by a simple ion

18 exchange process involving the cationic Zr tetramer and commonly-available macroporous

19 sulphonated polystyrene-divinylbenzene cation exchange resins, with subsequent

20 carbothermal reduction at 1350 °C. The materials were extensively characterised with respect

21 to composition, chemical structure and porosity. Carbothermal reduction of the Zr-loaded

22 templates resulted in formation of crystallites of the MAX phase zirconium sulphide carbide

23 (Zr₂SC) embedded within a highly microporous carbon framework with a macroporous

1

24   secondary structure inherited from the resin template. Despite the high BET surface areas of

25   the Zr$_2$SC-carbon composite microspheres (in some cases, greater than 600 m^2 g^{-1}), they are

26   extremely mechanically robust. The microspheres displayed high adsorption selectivity for

27   oxoanions relative to cationic solution species, including perrhenate (ReO$_4^-$), a pertechnetate

28   (TcO$_4^-$) surrogate. Accumulation of ReO$_4^-$ on the Zr$_2$SC particles was unequivocally

29   demonstrated by elemental mapping. Such materials are potential candidates as combined

30   ^{99}Tc sorbents and reusable transmutation hosts.

31   **Keywords**: technetium; adsorption; MAX phase; carbonization; ion exchange resin

32

1   Introduction

34   Nuclear power generation has produced as by-products, large inventories of fissile and

35   burnable extremely long-lived isotopes of the transuranic elements (Np, Pu, Am and Cm) as

36   well as long-lived fission products, including, but not limited to, ^{99}Tc, ^{93}Zr, ^{135}Cs, ^{107}Pd and

37   ^{129}I) [1, 2]. The above mentioned transuranics together are responsible for long-term decay

38   heat generation and radiotoxicity. Along with waste partitioning, one means of reducing

39   waste volume and long-term radiotoxicity that has been receiving serious consideration, is

40   transmutation via neutron irradiation, in order to convert long-lived radionuclides into much

41   shorter-lived ones. With respect to the latter initiative, the Gen IV International Forum has

42   selected next-generation reactor types for further R&D, with a goal of a closed nuclear fuel

43   cycle incorporating total actinide burn-up [3]. The irradiation matrix is often conceived as a

44   radiation-tolerant ceramic phase incorporating the Minor Actinides (Np, Am, Cm) in a solid

45   solution or mixture in the form of a fully-dense monolith, *viz.*, Inert Matrix Fuel (IMF). The

46   demands on a host matrix in terms of materials properties can best be described as extreme

47   and include very high melting point, thermal conductivity, chemical and radiation stability as

48   well as low neutron cross-section. Candidate host matrices include oxide, nitride and carbide

49   ceramics, as well as other mineral-based structures such as $Y_3Al_2O_5$ (yttrium aluminium

50   garnet or YAG) and spinel ($MgSi_2O_4$) [4]. For instance in the ECRIX-H experiment utilising

51   an Am-containing MgO matrix, a transmutation rate of 95% was achieved following

52   irradiation in the Phénix reactor with 29% fast flux for 318 effective full power days [5].

53   Nevertheless many technical challenges need to be overcome before Minor Actinide

54   transmutation can be implemented. Of the long-lived fission products, the transmutation of

55   ^{99}Tc, ($^{99}Tc + n \rightarrow {}^{100}Ru + \beta^-$) is generally considered technically feasible, although it has

56   received much less attention [1, 6]. The current work attempts to address target materials for

57   the transmutation of ^{99}Tc.

58   Conventional IMFs are dense single- or two-phase monolithic materials. A single phase

59   system would consist of the radionuclide to be transmuted being incorporated substitutionally

60   within the crystal structure of a ceramic phase. In two-phase systems such as ceramic-ceramic

61   (cercer) or cermic-metallic (cermet) composites the radionuclide is incorporated within a

62   separate phase. For instance, the ECRIX matrices are cercers since they initially consist of

63    $AmO_{1.62}$ particles dispersed in MgO [5]. However, most nuclear fuels have limited burn-up

64   capabilities, and only a fraction (say up to 30%) of the transuranics can be burned before the

65   fuel reaches its damage limits and needs to be reprocessed and refabricated. Therefore

66   reprocessability is an important criterion in determining the utility of a transmutation matrix

67   or fuel. In contrast, wasteform matrices for the immobilization of transuranics are required be

68   extremely insoluble under a wide range of potential geological conditions.

69   As an alternative to fully-dense transmutation targets, the dissolution of which might be

70   difficult, we suggested in our previous work that the aforementioned candidate host materials

71   prepared in suitable porous forms could be the basis for radiation-tolerant and reusable

72   targets, but with generation of less solid waste [7]. Porous monoliths would have several

73   potential advantages. First, fission gas generation would be less likely to cause swelling and

74   cracking since the gas could easily be accommodated within pores. Second, high energy

75   fragments resulting from neutronic reactions would always reside near pores. Third, the

76   reactants and products could be introduced and removed by simple solid-liquid phase

77   adsorption and desorption, respectively; and if the materials were prepared in granular forms,

78   could readily lend themselves to column chromatography. Such materials might also find

79   application in the production of nuclear medicines, wherein the easy recycling of costly

80   isotopically-enriched target elements would be desirable to minimise production costs. To

81   this end, we had produced carbon-zirconium carbide composite porous monoliths based on a

82   porous polyacrylonitrile (PAN) sphere template, with demonstrated reversible adsorption of

83   Mo. As one member of the aforementioned candidate transmutation matrices, zirconium

84   carbide (ZrC_{1-x}) possesses excellent thermal conductivity, radiation tolerance and thermal

85   stability [8].

86   Sorbents for ^{99}Tc have generally included diverse materials such activated carbon, natural

87   minerals, synthetic inorganics and ion exchange resins [9-22]. Metal-Organic Frameworks

88   (MOFs) have also been highlighted for their potential for ^{99}Tc removal and sequestration [23-

89   26]. There have been few examples of porous granular materials for ^{99}Tc capture and

90   especially ones well-suited to demanding radiation environments [27]. However, recently Shu

91   and co-workers reported ion-imprinted inorganic-based magnetic microspheres exhibiting

92   selectivity for ReO_4^- ([99]TcO_4^- surrogate) even in moderately acidic conditions [28].

93   The $M_{n+1}AX_n$ (MAX) phases are a relatively new family of layered, machinable, ternary

94   carbides and nitrides; where M is an early transition metal; A is one of the elements in groups

95   13–16; and *X* is C and/or N [29, 30]. Due to their oxidation resistance and other properties

96   there has been considerable interest in their potential as nuclear structural materials. They are

97   normally prepared at high temperatures under reducing conditions and are usually obtained as

98   dense monoliths of little use as adsorbents. However, it has been demonstrated that

99   exfoliation of the MAX phases can yield two-dimensional MXenes (analogous to graphene)

100   with cation intercalation properties [31, 32]. In this work, we report new porous composites

101   containing the Zr_2SC MAX phase, which were fabricated by a straightforward ion exchange-

102   based procedure promoting intimate contact between cationic Zr and polymeric organic

103   cation exchange resins. The latter serve as both porous structural templates and reactive

104   carbon sources, for *in situ* carbide formation via carbothermal reduction. Although metal-

105   loaded ion exchange resins have been employed as precursors for a diverse range of carbon

106   composites with ceramics and metals [33-44], to date this synthetic strategy has only been

107   applied to produce carbides of U and Si [45, 46].

108   The objective of the current work was to produce novel porous microspheres, which could

109   conceivably be utilised as radiation-tolerant sorbents for the selective capture of ^{99}Tc and its

110   subsequent transmutation. We detail the synthesis of these materials; determine their

111   compositions as well as their chemical and physical structural characteristics; and investigate

112   their adsorption properties.

113

2   Experimental

2.1   Materials

All chemical reagents including strong cation exchange resins were used as received without further purification. Dowex® DR-2030 H, Amberlyst® 15 H, Dowex® 50WX2 H and Amberlite® IR120 H and $ZrOCl_2.8H_2O$ (98%) were sourced from Sigma Aldrich, Australia. Duolite® C 255 H was obtained from Dia-prosim Limited, UK, while $NaReO_4$ (99.9%) was obtained from Strem Chemicals, USA. Trace metal analytical grade 69% HNO_3 was sourced from Seastar Chemicals Inc, Canada and Merck, Australia; and analytical grade 50 wt% NaOH solution was procured from Fluka Chemicals, Australia. A custom multi-element standard (2% HNO_3 matrix, > 99.96% purity) was supplied by High Purity Standards, USA. This solution was 10 mg L^{-1} with respect to each element and included Al, As, Ba, Be, B, Cd, Ca, Ce, Cs, Cr, Co, Cu, Dy, Er, Eu, Gd, Ga, Ho, Fe, La, Pb, Lu, Mg, Mn, Nd, Ni, P, K, Pr, Re, Rb, Sm, Se, Na, Sr, Tl, Tm, U, V, Yb and Zn. Instrument-grade air and 3.5 mol% H_2 in Ar gas mix were both produced by Coregas, Australia. Milli-Q® water (18.2 MΩ.cm) was used in all experiments.

2.2   Synthesis

2.2.1   Nomenclature

Zirconium-loaded resins were named ZrCX-1 to -5 to indicate the substrates used; these were: macroporous resins Dowex® DR-2030 and Amberlyst® 15 (ZrCX-1 and -2, respectively) and gel resins Dowex® 50WX2, Amberlite® IR-120 and Duolite® C255 (ZrCX-

6

134   3 to -5, respectively). Substrates were all sulphonated polystyrene-divinylbenzene strong

135   cation exchange resins (more specifications are given in Table S1).

136   **2.2.2   Zr adsorption**

137   Resins were loaded with aqueous $ZrOCl_2$ solutions using a batch contact time of one day and

138   mild agitation provided by a platform shaker (IKA, Germany). Macroporous resins were

139   loaded with volume-to-mass ratio (V/m) of 50 mL g^{-1} and 0.042 mol L^{-1} $ZrOCl_2$, while for

140   gel resins, V/m of 1 mL g^{-1} and 2.8 mol L^{-1} $ZrOCl_2$ were used. Loaded resins were collected

141   under suction, washed with Milli-Q® water and leached for one day to remove un-adsorbed

142   Zr. The leached resins were re-rinsed, air-dried overnight under suction and vacuum-dried

143   overnight at 60 °C (Thermo Electron, Germany).

144   **2.2.3   Thermal treatment**

145   Detailed conditions for carbothermal reduction were described in our previous work [7].

146   Briefly, the samples were heated in a graphite boat with lid in an alumina tube furnace under

147   a flow of 3.5 mol% H_2 in Ar mix and 24 hour residence time at any specified temperature.

148   Heat treatment at 1350 °C, being the maximum temperature achievable by the tube furnace,

149   was the standard procedure. Sample codes denote the 1350 °C-heated materials, unless

150   explicitly stated otherwise.

151   **2.3   Characterisation**

152   Thermogravimetric analysis (TGA) of samples (vacuum-dried overnight at 100 °C) was

153   conducted with a Seiko Instruments Inc. EXSTAR6000 thermal analyser under instrument air

154   carrier. Optical images were obtained with a Wild M400 optical macroscope. Secondary

155   electron images of microsphere fractured surfaces (2–3 nm Pt coated) were acquired with a

156   Zeiss Ultra Plus Scanning Electron Microscope (SEM). Scanning Transmission Electron

157   Microscopy (STEM) images and Energy Dispersive Spectroscopy (EDS) spectra were

158   acquired using a JEOL 2200FS operated at 200 keV. STEM specimens consisted of crushed

159   grains mixed with ethanol and dispersed on holey carbon films supported on TEM Cu mesh

160   grids. Nitrogen adsorption-desorption isotherms of samples (vacuum-degassed at 150 °C)

161   were acquired at 77 K (-196 °C) on a Micromeritics ASAP 2020 instrument. Mercury

162   intrusion profiles were obtained with a Micromeritics Autosorb IV 9520 Mercury

163   Porosimeter. Total surface areas were calculated with the Brunauer-Emmett-Teller (BET)

164   equation; micropore and external surface areas using a t-plot method; and pore size

165   distributions with a Density Functional Theory (DFT), N_2 on carbon slit pore model. Powder

166   X-Ray Diffraction (XRD) patterns were acquired with a PANalytical X'pert Pro X-Ray

167   Diffractometer using Cu weighted Kα radiation 1.5406 / 1.5444 Å 2:1, a step size of 0.0334

168   °2θ and an effective scan step time of 624.965 s. Rietveld Analysis of Zr_2SC was performed

169   using Rietica software (Version 2.1), employing a Newton-Raphson refinement strategy.

170   Profile fitting was conducted with a pseudo-Voigt function, while backgrounds were fitted

171   with a fifth order polynomial function. For Neutron Activation Analysis (NAA), neutron

172   irradiation was conducted at the OPAL Research Reactor, Lucas Heights, Australia, in a

173   thermal neutron flux of 2.2×10^{13} cm^{-2} s^{-1} for five minutes. Gamma spectra were acquired

174   using high purity Ge gamma detectors (P-type, 25% relative efficiency). Standardisation was

175   achieved using the k_0-method and certified gold wires standards [47]. Microanalysis of O

176   content was performed using a routine inert gas fusion method and employing a LECO

177   TCH600 instrument. All samples for NAA and O microanalysis were first vacuum-dried

178   overnight at 100 °C and vials backfilled with N_2. Raman spectra were collected using a

179   Renishaw inVia Raman spectrometer equipped with a Peltier-cooled CCD detector and set up

180   with either argon (514 nm) or HeCd (325 nm) laser excitation. The carbon in-plane crystallite

181   size was calculated using a general expression (Eq. 1) taking into account the laser

182   wavelength:

$$L_a = (2.4 \times 10^{-10}) \lambda_{laser}^4 \left(\frac{I_D}{I_G}\right)^{-1} \tag{1}$$

183   where L_a is the in-plane crystallite size (nm), λ_{laser} is the laser wavelength (nm), I_D is the D

184   peak intensity and I_G is the G peak intensity [48]. Individual whole microspheres were

185   mechanically tested between two metal flats (load cell and stationary surface) using an

186   Instron 5967 instrument with 500 N load cell, employing a compression rate of 0.01 mm

187   min^{-1}.

2.4   Adsorption studies

2.4.1   Solution preparation

190   For a pH 2 elemental selectivity profile, a 0.1 mg L^{-1} cocktail (with respect to each element)

191   was produced by diluting a multi-element custom standard 100-fold into pH 2.5 nitric acid

192   solution, with pH adjustment carried out by addition of aqueous HNO_3, employing magnetic

193   stirring.

194   For pH dependence studies, a solution 10 mg L^{-1} with respect to Re was produced by

195   dissolution of $NaReO_4$ in Milli-Q® water. With vigorous magnetic stirring, this was pH

196   adjusted with aqueous HNO_3 or NaOH solutions to produce subsamples of various pH values.

197   Each solution was aged for a day and its final pH measured.

198   For Re capacity measurements, STEM-EDS studies of Re loading and temperature

199   dependence, a 25 mg L^{-1} Re solution was produced by dissolution of $NaReO_4$ in Milli-Q®

200   water, with adjustment to pH 5 with dilute aqueous HNO_3 and employing magnetic stirring.

201   Aged overnight, the pH change was negligible. For kinetics and reuse, 1 mg L^{-1} (pH 5) and

202   10 mg L^{-1} (pH 3) Re solutions, respectively, were prepared similarly.

2.4.2   Contact experiments

204   Batch contact was conducted at about 20 °C with gentle agitation provided by a platform

205   shaker (IKA, Germany), except for temperature dependence measurements, which were

206   performed in a temperature-controlled shaker oven (WTC Binder, Germany).

207   The pH 2 selectivity survey was performed in triplicate at volume-to-mass ratio (V/m) of 200

208   mL g^{-1} with a contact time of one day. Supernatants were filtered through hydrophilic 0.45

209   µm syringe filters (Sartorius). Measurements of pH dependence were performed similarly,

210   but with a contact time of three days.

211   For capacity measurements, single solid portions were contacted for four days, with V/m

212   varied between 50 and 1000 mL g^{-1}. Subsampling of supernatants was conducted by pipette.

213   Re-loading of pre-ground STEM-EDS specimen was executed similarly, but with V/m of

214   2000 mL g^{-1}.

215   Kinetics measurements were performed in triplicate at V/m of 200 mL g^{-1}, with time varied

216   between 15 minutes and four days. Supernatants were subsampled by pipette.

217   For reuse studies, adsorption-desorption cycling was effected by changes in HNO_3

218   concentration. A single solid portion was contacted with 10 mg L^{-1} Re solution (pH 3) at V/m

219   of 200 mL g^{-1} for four days, with subsampling by pipette. The remaining supernatant was

220   removed and replaced with HNO_3 solution (pH 0), with subsequent contact for four days,

221   followed by subsampling by pipette. This procedure was repeated for two full cycles.

222   Between cycles, the solid material was washed and then leached (V/m of 5000 mL g^{-1}) with

223   Milli-Q® water for three days, to remove residual HNO$_3$.

224   Temperature dependence studies were carried out in triplicate with contact at V/m of 200 mL

225   g^{-1} for four days, sequentially at 30, 40 and 50 °C, respectively. Supernatants were removed

226   by pipette and cooled to room temperature prior to dilution for ICP-MS analysis.

227   Elemental analyses of supernatants and stocks were performed on an Agilent 7900 ICP Mass

228   Spectrometer. Values of % extraction were calculated using Eq. 2:

$$\% \ extraction \ = \ \frac{C_i - C_e}{C_i} \times 100 \tag{2}$$

229   and uptakes were calculated with Eq. 3 and 4:

$$q_e = \frac{(C_i - C_e)V}{m} \tag{3}$$

$$q_t = \frac{(C_i - C_t)V}{m} \tag{4}$$

230   where C_i is initial concentration (mg L^{-1}), C_e is equilibrium concentration (mg L^{-1}), C_t is

231   concentration (mg L^{-1}) at time t, q_e is the equilibrium amount adsorbed (mg g^{-1}), q_t is the

232   amount adsorbed (mg g^{-1}) at time t, V is volume (L) and m is mass of sorbent (g). Triplicates

233   were averaged and errors estimated from two sample standard deviations of each triplicate

234   set.

235   2.4.3   Model fitting and calculations

236   Details of standard calculations for fitting adsorption models, as well as thermodynamic

237   calculations, are given in Supplementary Material.

238

3   Results and Discussion

3.1   Loading of resins

241   The Zr uptake of the various cation exchange resins exhibited considerable variation. While

242   the macroporous resins (ZrCX-1 and -2 precursors) were readily saturated with dilute $ZrOCl_2$

243   solution (0.042 mol L^{-1}) (Table S2), loading of the gel resins (ZrCX-3 to -5 precursors) was

244   only satisfactorily achieved with concentrated solutions (2.8 mol L^{-1}). From TGA of the

245   loaded resins (Fig. S1), the refractory residues (presumed to be ZrO_2) were calculated to

246   verify successful loading with Zr. For ZrCX-1 to -5, these were 24.3, 25.0, 28.5, 10.6 and

247   10.4 wt%, respectively.

248

3.2   Effect of thermal treatment

250   Carbothermal reduction products of the Zr-loaded resins at 1350 °C were typically lustrous

251   black and highly spherical microspheres. A typical example, ZrCX-1, is presented in Fig. 1

252   (images of all materials are supplied in Fig. S2). Upon heating, the specimens exhibited

253   noticeable shrinkage compared to the precursors. The measured BET surface areas for ZrCX-

254   1 to -5 were 609, 626, 401, 7.1 and 7.5 m^2 g^{-1}, respectively. Thus, high Zr content seemed to

255   have a positive influence on surface area; the three loaded resins with much higher Zr content

256   (ZrCX-1 to -3) gave very high BET surface areas.

3.3 Composition and chemical structure

Elemental compositions of the thermally-treated microspheres were determined mainly using NAA and supplemented with O microanalysis (Table 1). From NAA, the main constituents were Zr, S, Hf and Na, with the remainder presumed to be mainly C and O. Traces of Cl, Mg, Al, V, Mn, Co and Cs were also found (data not shown). The trends in measured Zr concentrations agreed well with those seen earlier in the TGA of unheated Zr-loaded resins. The presence of Hf was anticipated as it is a common impurity in Zr, due to the difficulty in separating these two elements. The source of Na content was uncertain, however it could indicate that the starting resins were prepared in their Na forms and converted to H forms later on. Considerable O content (4.19–12.7%) was also found. The O in the Zr-loaded precursors originated from both sulphonate ($-SO_3H$) and zirconyl ($[Zr_4(OH)_8]^{8+}$) moieties; the naked polymer frameworks do not contain it. The compositional remainders (42–75.5 wt%), were inferred to be mainly C, making up the porous frameworks and the majority component in four out of the five materials.

Powder XRD patterns for ZrCX-1 to -5 are presented in Fig. 2a. Despite initial expectations of producing ZrC, the three high surface area materials, ZrCX-1 to -3, showed the same distinct reflections of a crystalline phase identified as the MAX phase zirconium sulphide carbide (Zr_2SC) [29, 30]. The Zr_2SC phase is known to have a $P6_3/mmc$ (hexagonal) space group [30]. The other two materials displayed broad irregular shaped bumps which were interpreted as amorphous content or very short-range order. Using Rietveld Analysis, attempts were made at fitting a hexagonal structure model to the data. Fitting background functions proved challenging due to the high background. Use of a beam knife did not improve this situation (data not shown) and it was concluded that the backgrounds was due to amorphous content. Despite this difficulty, peak positions were accurately fitted and lattice

13

281   parameters calculated. The a and c cell dimensions (Å) for Zr_2SC in ZrCX-1 to -3 were,

282   respectively: 3.416 ± 0.002, 12.143 ± 0.007; 3.417 ± 0.004, 12.150 ± 0.014; and $3.423 \pm$

283   0.013, 12.16 ± 0.04. These agreed well with previously reported values for this particular

284   MAX phase (summarised in Table S3) [49-57]. Interestingly, the Zr-to-S molar ratios

285   calculated from the compositional data above, ranged from 0.9 to 1.3; less than the 2:1

286   proportions expected from the Zr_2SC formula. The Zr-to-C molar ratios ranged from about

287   0.02 to 0.1, indicating that C was in vast excess. However, given the close agreement in

288   lattice dimensions to prior examples, a deviation in stoichiometry of the MAX phase seems

289   unlikely.

290   The carbon phases of ZrCX-1 to -3 were characterised by Raman Spectroscopy. Visible and

291   UV excitation Raman spectra for ZrCX-1 are shown (Fig. 2b); those of the other two

292   materials were highly similar and are given in Fig. S3. First, the absence of a discernible T

293   peak (~ 1060 cm^{-1}) in the 325 nm (UV excitation) spectrum demonstrated that sp^3-hybridised

294   carbon content was insignificant. The G peak (~ 1600 cm^{-1}) was unambiguous evidence of a

295   ringed sp^2 carbon structure. Furthermore, the G peak did not disperse (that is, change of peak

296   position as a function of laser excitation frequency), but only the D peak dispersed; this is

297   seen only in ordered carbons such as graphite, nanocrystalline graphite and glass-like carbon

298   [58]. Thus the carbon component of the composites appears to consist of a well-ordered

299   ringed sp^2 carbon structure, with relatively few defects.

300   The 2D (overtone) peak provides information about stacking order of sp^2 carbon sheets. In

301   highly-graphitised carbon, a fine structure is observed [48]. This was absent in the 2D peak of

302   the 514 nm spectrum of ZrCX-1, which instead showed a single smooth symmetrical peak.

303   This was thus evidence of disordered stacking or turbostraticity of the carbon sheets similar

304   to the so-called non-graphitic carbons [59]. An equally valid interpretation would be that the

305   sheets were randomly positioned in space, relative to one other.

306   Summarising, while there was evidence of an ordered ringed sp^2 graphene-like motif in

307   ZrCX-1, the carbon matrix exhibited a disordered three-dimensional structure.

308   **3.4   Porosity**

309   The internal pore structures of the materials were investigated with SEM. In the two

310   macroporous resin-derived materials, ZrCX-1 and -2 (Fig. 3a–d), no large macropores (i.e.

311   pores of the order of tens to hundreds of micrometres in diameter) could be observed. At

312   higher magnification, irregular coral-shaped polymer structures were observed in both

313   materials, surrounded by sub-micrometre macropores. Smaller gaps between adjacent

314   branches could be interpreted as mesopores. The gel resin-derived microspheres, ZrCX-3 to -

315   5 (Fig. 3e-j), were also lacking in large macropores, but somewhat smoother surface textures

316   were observed at higher magnification. Thus, these latter materials did not have the small

317   meso- and macropore architectures of the macroporous resin-derived microspheres. While

318   some evident loose surface fragments were noted in two of the images, these were probably

319   artefacts of the sample preparation.

320   The high surface area materials ZrCX-1 to -3 were examined by Nitrogen Porosimetry.

321   Adsorption-desorption isotherms of these materials are presented in Fig. 4a. All three Zr-

322   loaded resins developed considerable microporosity on heating, manifested as low relative

323   pressure branches characteristic of the Type I adsorption isotherm [60]. However, the

324   unloaded parent resins (Dowex® DR-2030, Amberlyst® 15 and Dowex® 50WX2,

325   respectively) upon similar heating, gave much lower surface areas of 25, 59 and $< 1 \ \mathrm{m^2 \ g^{-1}}$,

326   respectively. This implied that the inorganic portion played a role in the development of

327   microporosity and also that volatilisation of carbonaceous material could be ruled out as a

328   cause. The two macroporous resin-derived materials retained considerable

329   mesoporous/macroporous character of their parents, in contrast to the gel resin, which

330   collapsed on heating to yield a non-porous product whose surface area was too low to

331   accurately measure.

332   While the gel resin-derived ZrCX-3 exhibited a pure Type I isotherm, in ZrCX-1 and ZrCX-2

333   Type IV hysteresis loops were also observed, indicative of mesoporosity [60]. The hystereses

334   displayed reasonably flat plateaux, suggesting complete mesopore filling and the absence of

335   substantial macropore and/or external surface areas which would be manifested as Type II-

336   shaped features at relative pressures approaching unity [60]. The DFT pore size distributions

337   for ZrCX-1 to -3 (Fig. 4b), confirmed a mixture of micro- and large mesopores for both

338   ZrCX-1 and ZrCX-2 and only micropores for ZrCX-3. The former type of hierarchical

339   porosity would be highly desirable in order to facilitate mass transport.

340   Mercury Intrusion Porosimetry of whole microspheres was also undertaken (Fig. S4), but was

341   largely uninformative with respect to macropores. Apart from intrusion of interstitial

342   porosity, only mesopore openings were revealed; this thus demonstrated that the microsphere

343   surfaces were mesoporous.

344   **3.5   Mechanical testing**

345   Compressive strength testing of ZrCX-1 to -5 microspheres was conducted. Material ZrCX-1

346   was exceedingly robust with an average failure point of 38.3 N and sample standard deviation

347   of 6.3 N (n = 10). The microspheres shattered upon failure. A representative profile is given

348   in Fig. S5. The smaller-sized ZrCX-3 behaved similarly, with an average failure point of 24.7

349   N and sample standard deviation of 4.8 N (n = 10). The two low surface area materials also

350 proved to be mechanically strong and exhibited similar-shaped profiles, but also wide-

351 ranging variation in mechanical strength. ZrCX-4 yielded an average failure point of 26.0 N

352 and sample standard deviation of 19.0 N (n = 12), while ZrCX-5, the most robust of the

353 series, gave an average failure point of 109.7 N and sample standard deviation of 62.3 N (n =

354 10). However, the compression behaviour for material ZrCX-2 (n = 11) was not reproducible

355 with respect to profile shapes or failure points (data not shown), probably on account of the

356 significant proportion of irregular-shaped microsphere fragments. Based on the brittle (albeit

357 strong) overall nature of the materials and earlier presented Raman data, we would suggest

358 that the carbon frameworks are probably akin to glass-like carbon.

359 Considering that a typical ZrCX-1 microsphere weighed approximately 0.1 mg, it follows

360 that the same could withstand a compressive force equivalent to approximately 40 million

361 times its own weight (assuming g of 9.81 m s^{-2}). Therefore, mechanical strength should be no

362 limitation for deployment in separation applications, such as in columns, batch contact or

363 fluidised beds. In comparison, Drisko and co-workers produced fairly robust hierarchically

364 porous zirconium titanium oxide beads which could withstand up to 0.57 N [61].

365 **3.6   Structural evolution with temperature**

366 Based on its combination of favourable properties including multi-scale porosity, high

367 surface area and mechanical strength, ZrCX-1 was selected for the further study of its

368 structural evolution with temperature (Fig. 5). From XRD data, a crystalline phase identified

369 as tetragonal ZrO_2 (tZrO_2) had formed by 450 °C, which generally grew in intensity with

370 increasing temperature (Fig. S6a). By 1150 °C, the peak intensity of tZrO_2 had diminished

371 somewhat and from around 1250 °C, the hexagonal MAX phase Zr_2SC appeared which had

372 increased in intensity by 1350 °C (Fig 5a).

373 Surface area changes were monitored from 350–1350 °C (Fig. 5b; the complete set of

374 associated adsorption-desorption isotherms are given in Fig. S6b and c). The low external

375 surface areas for all temperatures confirmed that most of the BET surface area was associated

376 with micropore content. While it would be tempting to attribute microporosity to the

377 interstices between crystallites, or between crystallites and the carbon phase, the surface area

378 changes did not always correlate with the appearance or disappearance of the crystalline

379 phases. As examples, at 950 °C a large drop in surface area was seen even though no new

380 crystalline phase had appeared; and at the intermediate stage of 1150 °C, surface area

381 increased dramatically despite the absence of a well-defined crystalline phase. Instead, we

382 postulate that surface area increases were due to the reaction of volatile oxygen with carbon

383 *in situ* and/or voids left in the carbon phase by reaction with the inorganic phases.

384 Conversely, surface area losses were due to consolidation of groups of smaller pores to form

385 larger ones. One might consider this a form of activation, although any O-containing

386 functionalities generated on the carbon surface would likely be removed by the reducing and

387 carburising conditions.

388 Calculation of carbon in-plane crystallite size, L_a, for 550 – 1350 °C (Fig. 5c) revealed an

389 almost linear downward relationship with temperature. Intuitively, one might expect

390 carbonisation to give the opposite result, that is, coalescence of carbon domains, for example,

391 as displayed by polyacrylonitrile [62]. These observations, however, are consistent with

392 reactive carbon removal (postulated above) giving rise to increasingly tenuous connections

393 between carbon domains and statistically, the semblance of smaller average crystallite sizes.

394 Taken together, these characterisation data support a hypothesis of micropore generation

395 within the carbon phase. By extension, this explanation probably also accounts for the high

18

396 surface areas of the other two MAX phase-containing materials; and the low surfaces of the

397 two materials, ZrCX-4 and -5, in which the Zr_2SC phase did not form.

398

399 **3.7   Adsorption properties**

400 The adsorption properties of ZrCX-1 were scoped for a large suite of 41 elements at pH 2

401 (please refer to § 2.1 Materials for the full list). The material showed significant extraction

402 only of oxospecies-forming elements, As ($94 \pm 4\%$), Se ($93 \pm 4\%$), Re ($87 \pm 7\%$) and P (>

403 95%), with no discernible cation adsorption. Both Se and Re exist under these conditions of

404 pH and concentration as oxoanions, although interestingly, As(V) and P(V) are found

405 predominantly as the neutral species, arsenic acid (H_3AsO_4) and phosphoric acid (H_3PO_4)

406 [63, 64].

407 The adsorption of Re prompted us to consider ^{99}Tc as a credible adsorbate, given the close

408 similarity in chemistry between these two elements. Existing as the mononuclear tetrahedral

409 anionic species, perrhenate (ReO_4^-), Re is analogous to its cousin in Group 7, one period

410 above, Tc, which exists as pertechnetate (TcO_4^-) [64]. Thus, it is often regarded as a

411 surrogate to predict likely affinity for Tc. The adsorption of ReO_4^- as a function of pH was

412 further investigated for both ZrCX-1 as well as a carbon blank produced by heat-treating the

413 Dowex® DR-2030 parent resin in the same way (S.A._BET = $25 \text{ m}^2 \text{ g}^{-1}$) (Fig. 6a). Material

414 ZrCX-1 showed nearly quantitative extraction of ReO_4^- over the range of pH 3–10.5. By way

415 of comparison, the carbon blank only showed weak affinity, with discernible adsorption only

416 over the range of pH 1–5 and a maximum extraction of *ca.* 20% at pH 3. The adsorption

417 capacity of ZrCX-1 for ReO_4^- at pH 5 was also assessed (Fig. 6b). Isotherm model

418 parameters obtained from fitting to the experimental data are presented in Table 2. The

419   Freundlich model was a poor fit, with significant non-linearity evident in the data. The

420   Langmuir model fit, however, was considerably better. The calculated value of q_{max}

421   (adsorption capacity) for the latter model was a modest 13.85 mg g^{-1} (*ca.* 0.074 mmol g^{-1}),

422   which visually accorded well with the plotted isotherm data. Capacity of the carbon blank

423   was also surveyed at pH 5 for comparison and showed no measurable adsorption, in

424   agreement with the pH dependence discussed above. Since the high carbon micropore surface

425   area of ZrCX-1 was obviously underutilised, one avenue for increasing adsorption capacity

426   could be to activate this carbon surface by sulphonation; load additional Zr; and repeat

427   carbothermal reduction treatment.

428   The Re adsorption kinetics of ZrCX-1 were investigated (Fig. 6c). Fit parameters for the

429   pseudo-second-order model are presented in Table 3. Overall, the pseudo-second-order model

430   proved to be reasonable fit to the data. The kinetics were found to be be relatively slow, with

431   equilibrium only reached in 48–72 hours. Measured uptake at 24 hours was *ca.* 96% of q_e.

432   These results can probably be attributed to a lack of large macropores which would facilitate

433   fast intraparticle diffusion.

434   Measurements of temperature dependence of Re adsorption onto ZrCX-1 were undertaken to

435   quantify the associated thermodynamic parameters (Table 4). Increasing temperature had the

436   effect of reducing the K_d value (Fig. S8). Large negative values of ΔH° (enthalpy) and ΔG°

437   (Gibbs free energy) were calculated, clearly implying that the adsorption was an exothermic

438   and spontaneous process. The negative value of ΔS° (entropy) would indicate ordering at the

439   solid surface.

440   One might find the preceding fairly convincing evidence for the Zr_2SC phase supplying the

441   majority of adsorption sites. However, efforts were made to corroborate this directly by way

442   of microstructural chemical analysis. Elemental mapping of a portion of the Re-loaded ZrCX-

443 1 material was undertaken using STEM-EDS (Fig. 7). The bright field image of ZrCX-1 (Fig.

444 6a) exhibited dark inorganic particles suspended on the lighter-shaded carbon phase.

445 Mapping of Zr, S, O and Re elemental distributions (Fig. 7b–e, respectively) demonstrated

446 that these four elements were mainly associated with one another. Thus, this unequivocally

447 demonstrated that ReO_4^- accumulates upon the Zr_2SC aggregates/particles, with no

448 significant adsorption on the carbon phase. With reference to the earlier bulk compositional

449 data, these results also suggest that O and excess S are not associated with the carbon phase;

450 and in addition to the Zr_2SC itself, may be part of a secondary inorganic phase. Due to the

451 very small scale of the STEM specimen, however, it cannot be ruled out that there are

452 pockets of unreacted material within the bulk of the material, rendered inaccessible to the

453 carbothermal treatment by shrinkage of the resin precursor during heating. It is also possible

454 that some O is dissolved within the Zr_2SC lattice. This latter explanation is plausible, given

455 that other studies have shown that very high temperatures are required to completely remove

456 dissolved O from ZrC and HfC powders [65].

457 The adsorption results presented above, certainly do contrast with most previous studies of

458 MXenes, which typically show cation extraction; adsorption of alkali metals, alkaline earth

459 metals, Pb as well as U, have all been demonstrated [66-68]. It should be noted, however, that

460 Ying and co-workers reported affinity of $Ti_3C_2T_x$ (T = OH or F) for $Cr_2O_7^{2-}$, seemingly

461 attributable to protonated surface hydroxyl groups [69]. We postulate two mechanisms for Re

462 adsorption, which are not necessarily mutually exclusive. The first is a surface electrostatic

463 model involving attraction by regions of negative charge on high-electronegative O bound to

464 the adsorbate, to regions of positive charge on the carbide surface. This is a strong

465 hypothesis, as it should universally explain adsorption of neutral, anionic and cationic

466 oxospecies. We have also, in fact, observed the adsorption of cationic UO_2^{2+} above pH 3, as

467 well as neutral and anionic Mo species (H_2MoO_4, $HMoO_4^-$ and MoO_4^{2-}) (Fig. S7). In a

21

468   second scenario, it is conceivable that the "A layer" S terminating at the solid-liquid interface

469   is oxidised and anion-exchangeable by adsorbate molecules. If this second hypothesis is

470   applicable to any degree, one should expect a concomitant release of S into the surrounded

471   solution.

472   There have been relatively few studies on the neutron irradiation stability of MAX phases

473   [70-77]. Some phases such as the well-studied Ti_3SiC_2 and Ti_3AlC_2 appear to be reasonably

474   tolerant and may be candidate nuclear structural materials. There would seem to be evidence

475   supporting the role of the A layer in accommodating antisite defects, thus aiding in damage

476   recovery over amorphisation [71, 77]. The antisite formation energies are in turn, influenced

477   by the bonding overlap in the MX layer [71, 73]. The specific performance of Zr_2SC in these

478   respects is unknown. A further consideration is that the cited studies focus on changes to

479   mechanical properties; as to what influence structural damage (if any) might have on the

480   surface chemistry and observed adsorption properties is a question that remains to be

481   answered. Nonetheless, these previous investigations do hold some promise for the durability

482   of the ZrCX-1 sorbent, subjected to irradiation.

483   The reusability of ZrCX-1 was studied two complete adsorption-desorption cycles by varying

484   the HNO_3 concentration of the contact solution. For cycle one, 96% adsorption was observed

485   and 76% desorption; for cycle 2, 96% adsorption and 89% desorption. These preliminary

486   results show that the ReO_4^- adsorption is in principle reversible, although additional work

487   will be needed to establish optimal conditions.

488

4   Conclusions

The synthesis of new mechanically robust and highly porous microsphere composites of carbon and the hexagonal MAX phase Zr_2SC, based on a non-laborious procedure involving the carbothermal reduction of Zr-loaded common strong cation exchange resins has been demonstrated. The Zr loadings achieved varied among the resins and appeared to be an important factor in the development of high surface areas and formation of Zr_2SC, which were observed in one gel resin-derived and both macroporous resin-derived materials. Cell dimensions of this phase determined by Rietveld Method agreed well with prior published examples. It was concluded based on Raman data that the carbon phase consisted of ordered carbon sheets with disordered stacking or random orientation in space. Porosity was investigated in the three high surface area Zr_2SC-containing materials using SEM and Nitrogen Porosimetry. All had developed microporosity, while the two macroporous-resin derived materials additionally contained mesopores and small macropores originating from their substrate resins.

Of the three Zr_2SC-containing materials, ZrCX-1 was chosen for further study based on its combination of favourable properties including high surface area, mechanical strength and multi-scale porosity. For ZrCX-1, trends in crystallisation, surface area and carbon in-plane crystallite size as a function of temperature, together supported a hypothesis of micropore formation occurring within the carbon phase due to reactive carbon removal. This carbon phase is ostensibly a relative of glass-like carbon. This hypothesied mechanism probably also accounts for the high surface areas of the other two MAX-phase materials in the series.

Investigation of ZrCX-1 for adsorption selectivity at pH 2, showed affinity for oxospecies-forming elements, including As, Se, Re and P. Both neutral and anionic species were shown to adsorb, suggesting that an electrostatic interaction must play at least some role. Re was

513   then used as a surrogate in studies designed to anticipate the performance in extraction of

514   ^{99}Tc, a long-lived fission product in High Level Waste (HLW). Nearly quantitative extraction

515   over the range of pH 3–10.5 was demonstrated, with over 90% extraction observed from pH

516   2. Elemental mapping employing TEM-EDS confirmed the role of the Zr_2SC MAX phase in

517   the adsorption of ReO_4^-. The Langmuir model provided a superior fit to adsorption isotherm

518   data at pH 5, yielding a q_{max} constant (Langmuir adsorption capacity) of 13.85 mg g^{-1}. A

519   suggestion for further optimising this characteristic was offered. Likewise, adsorption

520   kinetics for ZrCX-1 were modelled by pseudo-second-order model and found to be relatively

521   slow (equilibrium reached in 48–72 hours), suggesting future opportunities for optimisation

522   of pore architecture. Thermodynamic measurements demonstrated that the adsorption process

523   was spontaneous and exothermic. The adsorption was also shown to be reversible, indicating

524   the possibility for recycling of the matrix.

525   Given the simplicity of their syntheses and porous granular natures affording potential use in

526   a chromatographic column, one might envisage one application being the deployment of the

527   materials for the direct selective extraction of ^{99}Tc from HLW and subsequent transmutation

528   with thermal neutrons. For instance, the microspheres could be packed into a column within a

529   Zr-alloyed housing, for convenient loading of ^{99}Tc, neutron irradiation and post-irradiation

530   elution of products. The microspheres are rigid and not subject to swelling effects, unlike

531   polymeric ion exchange resins and are not likely to be damaged by fission gas build-up.

532   Although radiation tolerance is anticipated, this will need to be evaluated for the Zr_2SC phase

533   to properly gauge practical lifespan in a real recycling scenario. That is to say, while prior

534   radiation damage studies of other MAX phases indicate good general stability for this class of

535   materials, the specific performance of the Zr_2SC MAX phase in high thermal neutron fluxes

536   would need to be addressed if it is to be considered for this application. This is a question we

537   are working towards answering.

24

552

Figures captions

554

555 Fig. 1. Optical microscopy image of ZrCX-1.

556 Fig. 2. (a) Powder XRD patterns. Key: h, hexagonal Zr_2SC; and (b) Raman spectra of ZrCX-

557 1, representative of ZrCX-1 to -3.

558   Fig. 3. SEM images of internal fractured microsphere surfaces at 1,000 and 50,000 ×

559   magnification. (a) and (b) ZrCX-1; (c) and (d) ZrCX-2; (e) and (f) ZrCX-3; (g) and (h) ZrCX-

560   4; and (i) and (j) ZrCX-5.

561   Fig. 4. Nitrogen Porosimetry data. (a) adsorption-desorption isotherms; and (b) pore size

562   distributions.

563   Fig. 5. Structural evolution of ZrCX-1 with temperature. (a) Powder XRD patterns. Key: t,

564   tetragonal ZrO_2; h, hexagonal Zr_2SC; (b) micropore, external and BET surface areas; and (c)

565   in-plane carbon crystallite sizes.

566   Fig. 6. Adsorption data. (a) pH dependence for ReO_4^- adsorption onto ZrCX-1 and a carbon

567   blank; (b) isotherm data for ReO_4^- adsorption onto ZrCX-1 at pH 5 with fitted Langmuir and

568   Freundlich models; and (c) kinetics data for ReO_4^- adsorption onto ZrCX-1 at pH 5 with

569   pseudo-second-order model fit.

570   Fig. 7. STEM studies of Re-loaded ZrCX-1. (a) Bright field image; and corresponding

571   STEM-EDS elemental maps (b–e) of Zr, S, O and Re distributions.

572

573   **Tables**

574   Table 1. Elemental compositions of ZrCX-1 to -5.

Material	Zr (wt%)	S (wt%)	O (wt%)	Hf (wt%)	Na (wt%)	Balance (wt%)
ZrCX-1	26 ± 2	6.9 ± 0.5	9.9 ± 0.2	0.58 ± 0.04	0.0043 ± 0.0003	57 ± 2
ZrCX-2	26 ± 2	8.0 ± 0.6	10.2 ± 0.2	0.57 ± 0.04	0.0051 ± 0.0004	55 ± 2
ZrCX-3	32 ± 2	12.2 ± 0.9	12.7 ± 0.3	0.75 ± 0.05	0.0179 ± 0.0013	42 ± 3

ZrCX-4	11.4 ± 0.8	8.6 ± 0.7	4.19 ± 0.08	0.27 ± 0.02	0.060 ± 0.004	75.5 ± 1.5
ZrCX-5	12.3 ± 0.9	9.6 ± 0.8	4.48 ± 0.09	0.29 ± 0.02	0.40 ± 0.03	73.0 ± 1.7

Table 2. Isotherm model fit parameters for ReO_4^- adsorption onto ZrCX-1 at pH 5.

Model	q_{max} (mg g^{-1})	b (L mg^{-1})	n	K_f (mg g^{-1})	R^2
Langmuir	13.85	1.59			0.993
Freundlich			2.97	6.56	0.949

Table 3. Kinetic model fit parameters for ReO_4^- adsorption onto ZrCX-1 at pH 5.

Model	q_e (mg g^{-1})	k_2 (g mg^{-1}h^{-1})	R^2
Pseudo-second-order	0.200	2.36	0.999

Table 4. Thermodynamic parameters for ReO_4^- adsorption onto ZrCX-1 at pH 5.

ΔS° (J K^{-1} mol^{-1})	ΔH° (kJ mol^{-1})	Temperature (°C)	ΔG° (kJ mol^{-1})
−109.0	−57.07	30	−24.01

40	−22.92
50	−21.83

585

586

587

588

References

590   [1] K. Kora, H. Nakaya, H. Matsuura, M. Goto, S. Nakagawa, S. Shimakawa, A study on
591   transmutation of LLFPs using various types of HTGRs, Nucl. Eng. Des., 300 (2016) 330-338.
592   [2] B.R. Bergelson, A.S. Gerasimov, G.V. Tikhomirov, Radiotoxicity and decay heat power
593   of spent nuclear fuel of VVER type reactors at long-term storage, Radiat Prot Dosimetry, 115
594   (2005) 445-447.
595   [3] A Technology Roadmap for Generation IV Nuclear Energy Systems, 2002.
596   [4] S. Pillon, Actinide-bearing fuels and transmutation targets, in: R.J.M. Konings (Ed.)
597   Comprehensive Nuclear Materials, Elsevier B.V., 2012, pp. 109-141.
598   [5] J. Lamontagne, Y. Pontillon, E. Esbelin, S. Bejaoui, B. Pasquet, P. Bourdot, J.M.
599   Bonnerot, Determining the americium transmutation rate and fission rate by post-irradiation
600   examination within the scope of the ECRIX-H experiment, J. Nucl. Mater., 440 (2013) 366-
601   376.
602   [6] M. Salvatores, I. Slessarev, A. Tchistiakov, The transmutation of long-lived fission
603   products by neutron irradiation, Nucl. Sci. Eng., 130 (1998) 309-319.
604   [7] N. Scales, J. Chen, T.L. Hanley, D.P. Riley, G.R. Lumpkin, V. Luca, Hierarchically
605   porous carbon-zirconium carbide spheres as potentially reusable transmutation targets,
606   Microporous Mesoporous Mater., 212 (2015) 100-109.
607   [8] Y. Katoh, G. Vasudevamurthy, T. Nozawa, L.L. Snead, Properties of zirconium carbide
608   for nuclear fuel applications, J. Nucl. Mater., 441 (2013) 718-742.
609   [9] B. Gu, K.E. Dowlen, L. Liang, J.L. Clausen, Efficient separation and recovery of
610   technetium-99 from contaminated groundwater, Sep. Technol., 6 (1996) 123-132.
611   [10] E. Holm, T. Gafvert, P. Lindahl, P. Roos, In situ sorption of technetium using activated
612   carbon, Appl. Radiat. Isot., 53 (2000) 153-157.
613   [11] Y.F. Wang, H.Z. Gao, R. Yeredla, H.F. Xu, M. Abrecht, Control of pertechnetate
614   sorption on activated carbon by surface functional groups, Journal of Colloid and Interface
615   Science, 305 (2007) 209-217.

28

616 [12] N.N. Popova, G.L. Bykov, G.A. Petukhova, I.G. Tananaev, B.G. Ershov, Sorption of
617 Tc(VII) and Am(III) by carbon materials: effect of oxidation, J. Radioanal. Nucl. Chem., 298
618 (2013) 1463-1468.
619 [13] H. Zhuang, J. Zeng, L. Zhu, Sorption of radionuclides technetium and iodine on
620 minerals, Radiochim. Acta, 44-45 (1988) 143-145.
621 [14] A. Winkler, H. Bruehl, C. Trapp, W.D. Bock, Mobility of technetium in various rocks
622 and defined combinations of natural minerals, Radiochim. Acta, 44-45 (1988) 183-186.
623 [15] S. El-Wear, K.E. German, V.F. Peretrukhin, Sorption of technetium on inorganic
624 sorbents and natural minerals, J. Radioanal. Nucl. Chem., 157 (1992) 3-14.
625 [16] L. Liang, B. Gu, X. Yin, Removal of technetium-99 from contaminated groundwater
626 with sorbents and reductive materials, Sep. Technol., 6 (1996) 111-122.
627 [17] M.J. Kang, S.W. Rhee, H. Moon, V. Neck, T. Fanghaenel, Sorption of MO_4- (M = Tc,
628 Re) on Mg/Al layered double hydroxide by anion exchange, Radiochim. Acta, 75 (1996) 169-
629 173.
630 [18] D.J. Liu, X.H. Fan, Adsorption behavior of 99Tc on Fe, Fe_2O_3 and Fe_2O_4, J. Radioanal.
631 Nucl. Chem., 264 (2005) 691-698.
632 [19] V. Peretroukhine, C. Sergeant, G. Deves, S. Poulain, M.H. Vesvres, B. Thomas, M.
633 Simonoff, Technetium sorption by stibnite from natural water, Radiochim. Acta, 94 (2006)
634 665-669.
635 [20] R. Koivula, R. Harjula, Selective sorption of technetium on antimony-doped tin dioxide,
636 Sep. Sci. Technol., 46 (2011) 315-320.
637 [21] G. Sheng, Y. Tang, W. Linghu, L. Wang, J. Li, H. Li, X. Wang, Y. Huang, Enhanced
638 immobilization of ReO_4- by nanoscale zerovalent iron supported on layered double
639 hydroxide via an advanced XAFS approach: Implications for TcO_4- sequestration, Appl.
640 Catal., B, 192 (2016) 268-276.
641 [22] I.E. Burgeson, J.R. Deschane, D.L. Blanchard, Jr., Removal of technetium from Hanford
642 tank waste supernates, Sep. Sci. Technol., 40 (2005) 201-223.
643 [23] H. Fei, D.L. Rogow, S.R.J. Oliver, Reversible Anion Exchange and Catalytic Properties
644 of Two Cationic Metal-Organic Frameworks Based on Cu(I) and Ag(I), J. Am. Chem. Soc.,
645 132 (2010) 7202-7209.
646 [24] R. Cao, B.D. McCarthy, S.J. Lippard, Immobilization, Trapping, and Anion Exchange of
647 Perrhenate Ion Using Copper-Based Tripodal Complexes, Inorg. Chem., 50 (2011) 9499-
648 9507.
649 [25] D. Sheng, L. Zhu, C. Xu, C. Xiao, Y. Wang, Y. Wang, L. Chen, J. Diwu, J. Chen, Z.
650 Chai, T.E. Albrecht-Schmitt, S. Wang, Efficient and Selective Uptake of TcO_4- by a Cationic
651 Metal-Organic Framework Material with Open Ag+ Sites, Environ. Sci. Technol., 51 (2017)
652 3471-3479.
653 [26] L. Zhu, C. Xiao, X. Dai, J. Li, D. Gui, D. Sheng, L. Chen, R. Zhou, Z. Chai, T.E.
654 Albrecht-Schmitt, S. Wang, Exceptional Perrhenate/Pertechnetate Uptake and Subsequent
655 Immobilization by a Low-Dimensional Cationic Coordination Polymer: Overcoming the
656 Hofmeister Bias Selectivity, Environ. Sci. Technol. Lett., 4 (2017) 316-322.
657 [27] D. Banerjee, W. Xu, Z. Nie, L.E.V. Johnson, C. Coghlan, M.L. Sushko, D. Kim, M.J.
658 Schweiger, A.A. Kruger, C.J. Doonan, P.K. Thallapally, Zirconium-Based Metal-Organic
659 Framework for Removal of Perrhenate from Water, Inorg. Chem., 55 (2016) 8241-8243.
660 [28] X. Shu, L. Shen, Y. Wei, D. Hua, Synthesis of surface ion-imprinted magnetic
661 microsphere for efficient sorption of perrhenate: A structural surrogate for pertechnetate, J.
662 Mol. Liq., 211 (2015) 621-627.
663 [29] H. Nowotny, W. Jeitschko, F. Benesovsky, Novel complex carbides and nitrides and
664 their relation to phases of hard substances, Planseeber. Pulvermetall., 12 (1964) 31-43.

665 [30] M.W. Barsoum, The MN+1AXN phases: a new class of solids; thermodynamically
666 stable nanolaminates, Prog. Solid State Chem., 28 (2000) 201-281.
667 [31] M. Naguib, M. Kurtoglu, V. Presser, J. Lu, J. Niu, M. Heon, L. Hultman, Y. Gogotsi,
668 M.W. Barsoum, Two-Dimensional Nanocrystals Produced by Exfoliation of Ti3AlC2, Adv.
669 Mater. (Weinheim, Ger.), 23 (2011) 4248-4253.
670 [32] M. Naguib, O. Mashtalir, J. Carle, V. Presser, J. Lu, L. Hultman, Y. Gogotsi, M.W.
671 Barsoum, Two-Dimensional Transition Metal Carbides, ACS Nano, 6 (2012) 1322-1331.
672 [33] K.F. Blurton, Preparation of highly dispersed platinum on carbon, Carbon, 10 (1972)
673 305-315.
674 [34] K. Miura, H. Nakagawa, Preparation of metal-loaded porous carbons and their use as a
675 highly active catalyst for reduction of nitric oxide (NO), in: E. Yasuda, M. Inagaki, K.
676 Kaneko, M. Endo, A. Oya, Y. Tanabe (Eds.) Carbon Alloys: Novel Concepts to Develop
677 Carbon Science and Technology, Elsevier Science Ltd., 2003, pp. 499-513.
678 [35] P. Trens, V. Caps, J.W. Peckett, Catalytic oxidation of trans-stilbene using pyrolysed
679 manganese-loaded cation exchange resin, Appl. Catal., A, 251 (2003) 19-28.
680 [36] P. Trens, J.W. Peckett, V.N. Stathopoulos, M.J. Hudson, P.J. Pomonis, Phosphotungstate
681 anions supported on spherical beads of carbon as highly efficient catalysts for the dehydration
682 of propan-2-ol to propene, Appl. Catal., A, 241 (2003) 217-226.
683 [37] B. Li, Y. Ren, Q. Fan, A. Feng, W. Dong, Preparation and characterization of spherical
684 nickel-doped carbonaceous resin as hydrogenation catalysts. I. Carbonization procedures,
685 Carbon, 42 (2004) 2669-2676.
686 [38] W. Yu, J. Zheng, X. He, Y. Zhao, Synthesis of spherical activated carbon loaded with
687 metal particles and its performance of thiophene adsorption, Huagong Xuebao (Chin. Ed.), 59
688 (2008) 2824-2829.
689 [39] W. Yu, Y. Zhang, T. Li, Y. Zhao, X. Qu, Y. Liu, S. Li, Spherical activated carbon
690 material loaded with metal, and preparation method and application thereof, CN101385966A,
691 2009.
692 [40] S. Kudo, T. Maki, K. Miura, K. Mae, High porous carbon with Cu/ZnO nanoparticles
693 made by the pyrolysis of carbon material as a catalyst for steam reforming of methanol and
694 dimethyl ether, Carbon, 48 (2010) 1186-1195.
695 [41] M.S. Wilson, A. Delariva, F.H. Garzon, Synthesis of sub-2 nm ceria crystallites in
696 carbon matrixes by simple pyrolysis of ion-exchange resins, J. Mater. Chem., 21 (2011)
697 7418-7424.
698 [42] L. Kotai, T. Pasinszki, Z. Czegeny, S. Balint, I. Sajo, Z. May, P. Nemeth, Z. Karoly,
699 P.K. Sharma, V. Sharma, K.K. Banerji, Metal and metal-sulfide containing carbons from
700 sulfonated styrene-divinylbenzene copolymer based ion-exchangers, Eur. Chem. Bull., 1
701 (2012) 398-400.
702 [43] W. Li, Z. Zhang, A. Cui, J. Fan, X. Sun, A gasoline desulfurization adsorbent and
703 preparation method thereof, CN103143321A, 2013.
704 [44] J. Fan, H. Lan, Z. Zhang, W. Li, Study on gasoline adsorptive desulfurization of resin-
705 based modified spherical activated carbon, Shiyou Lianzhi Yu Huagong, 45 (2014) 10-15.
706 [45] R.L. Beatty, Microspheres containing metal carbide from metal-charged resin beads,
707 DE2527093A1, 1976.
708 [46] L. Tosheva, J. Parmentier, S. Saadallah, C. Vix-Guterl, V. Valtchev, J. Patarin, Carbon
709 and SiC Macroscopic Beads from Ion-Exchange Resin Templates, J. Am. Chem. Soc., 126
710 (2004) 13624-13625.
711 [47] A. Simonits, F. De Corte, J. Hoste, Single-comparator methods in reactor neutron
712 activation analysis, J. Radioanal. Chem., 24 (1975) 31-46.

713   [48] M.A. Pimenta, G. Dresselhaus, M.S. Dresselhaus, L.G. Cancado, A. Jorio, R. Saito,
714   Studying disorder in graphite-based systems by Raman spectroscopy, Phys. Chem. Chem.
715   Phys., 9 (2007) 1276-1291.
716   [49] H. Kudielka, H. Rohde, Structural investigations of carbosulfides of titanium and
717   zirconium, Z. Kristallogr., Kristallgeom., Kristallphys., Kristallchem., 114 (1960) 447-456.
718   [50] A. Bouhemadou, R. Khenata, Structural, electronic and elastic properties of M2SC
719   (M=Ti, Zr, Hf) compounds, Phys. Lett. A, 372 (2008) 6448-6452.
720   [51] S.R. Kulkarni, N.A. Phatak, S.K. Saxena, Y. Fei, J. Hu, High pressure structural
721   behavior and synthesis of Zr2SC, J. Phys.: Condens. Matter, 20 (2008) 135211/135211-
722   135211/135216.
723   [52] M.F. Cover, O. Warschkow, M.M.M. Bilek, D.R. McKenzie, A comprehensive survey
724   of M2AX phase elastic properties, J. Phys.: Condens. Matter, 21 (2009) 305403/305401-
725   305403/305409.
726   [53] H. Fu, J. Yang, Z. Zhao, P. Feng, W. Liu, T. Gao, Static compressibility, thermal
727   expansion and elastic anisotropy of Zr2SC single crystals, Solid State Commun., 149 (2009)
728   2110-2114.
729   [54] W. Feng, S. Cui, H. Hu, P. Feng, Z. Zheng, Y. Guo, Z. Gong, First-principles study on
730   electronic structure and elastic properties of hexagonal Zr2SC, Phys. B (Amsterdam, Neth.),
731   405 (2010) 4294-4298.
732   [55] M.B. Kanoun, S. Goumri-Said, A.H. Reshak, A.E. Merad, Electro-structural
733   correlations, elastic and optical properties among the nanolaminated ternary carbides Zr2AC,
734   Solid State Sci., 12 (2010) 887-898.
735   [56] S. Cui, D. Wei, H. Hu, Z. Gong, Mechanical instability and ideal strengths of layered
736   M2SC (M = Ti, Zr, and Hf) compounds, J. Appl. Phys. (Melville, NY, U. S.), 113 (2013)
737   083516/083511-083516/083517.
738   [57] M.T. Nasir, M.A. Hadi, S.H. Naqib, F. Parvin, A.K.M.A. Islam, M. Roknuzzaman, M.S.
739   Ali, Zirconium metal-based MAX phases Zr2AC (A = Al, Si, P and S): A first-principles
740   study, Int. J. Mod. Phys. B, 28 (2014) 1550022/1550021-1550022/1550016.
741   [58] A.C. Ferrari, Raman spectroscopy of graphene and graphite: Disorder, electron-phonon
742   coupling, doping and nonadiabatic effects, Solid State Commun., 143 (2007) 47-57.
743   [59] R.E. Franklin, The structure of graphitic carbons, Acta Crystallogr., 4 (1951) 253-261.
744   [60] K.S.W. Sing, D.H. Everett, R.A.W. Haul, L. Moscou, R.A. Pierotti, J. Rouquerol, T.
745   Siemieniewska, Reporting physisorption data for gas/solid systems, Pure Appl. Chem., 57
746   (1985) 603-619.
747   [61] G.L. Drisko, K.M. Chee, N. Scales, A. Ide, E. Sizgek, R.A. Caruso, V. Luca, One-pot
748   preparation and uranyl adsorption properties of hierarchically porous zirconium titanium
749   oxide beads using phase separation processes to vary macropore morphology, Langmuir, 26
750   (2010) 17581-17588.
751   [62] M.S.A. Rahaman, A.F. Ismail, A. Mustafa, A review of heat treatment on
752   polyacrylonitrile fiber, Polymer Degradation and Stability, 92 (2007) 1421-1432.
753   [63] CRC Handbook of Chemistry and Physics, 96th ed., CRC Press, Boca Raton, 2015.
754   [64] C.F. Baes, R.E. Mesmer, The Hydrolysis of Cations, Robert E. Krieger Publishing
755   Company, Inc, Malabar.
756   [65] M.D. Sacks, C.-A. Wang, Z. Yang, A. Jain, Carbothermal reduction synthesis of
757   nanocrystalline zirconium carbide and hafnium carbide powders using solution-derived
758   precursors, J. Mater. Sci., 39 (2004) 6057-6066.
759   [66] Q. Peng, J. Guo, Q. Zhang, J. Xiang, B. Liu, A. Zhou, R. Liu, Y. Tian, Unique lead
760   adsorption behavior of activated hydroxyl group in two-dimensional titanium carbide, J Am
761   Chem Soc, 136 (2014) 4113-4116.

762 [67] M. Ghidiu, J. Halim, S. Kota, D. Bish, Y. Gogotsi, M.W. Barsoum, Ion-Exchange and
763 Cation Solvation Reactions in Ti3C2 MXene, Chem. Mater., 28 (2016) 3507-3514.
764 [68] L. Wang, L. Yuan, K. Chen, Y. Zhang, Q. Deng, S. Du, Q. Huang, L. Zheng, J. Zhang,
765 Z. Chai, M.W. Barsoum, X. Wang, W. Shi, Loading Actinides in Multilayered Structures for
766 Nuclear Waste Treatment: The First Case Study of Uranium Capture with Vanadium Carbide
767 MXene, ACS Appl. Mater. Interfaces, 8 (2016) 16396-16403.
768 [69] Y. Ying, Y. Liu, X. Wang, Y. Mao, W. Cao, P. Hu, X. Peng, Two-Dimensional
769 Titanium Carbide for Efficiently Reductive Removal of Highly Toxic Chromium(VI) from
770 Water, ACS Appl. Mater. Interfaces, 7 (2015) 1795-1803.
771 [70] E.N. Hoffman, D.W. Vinson, R.L. Sindelar, D.J. Tallman, G. Kohse, M.W. Barsoum,
772 MAX phase carbides and nitrides: Properties for future nuclear power plant in-core
773 applications and neutron transmutation analysis, Nucl. Eng. Des., 244 (2012) 17-24.
774 [71] S. Zhao, J. Xue, Y. Wang, Q. Huang, Ab initio study of irradiation tolerance for different
775 Mn+1AXn phases: Ti3SiC2 and Ti3AlC2, J. Appl. Phys. (Melville, NY, U. S.), 115 (2014)
776 023503/023501-023503/023509.
777 [72] D.J. Tallman, E.N. Hoffman, E.a.N. Caspi, B.L. Garcia-Diaz, G. Kohse, R.L. Sindelar,
778 M.W. Barsoum, Effect of neutron irradiation on select MAX phases, Acta Mater., 85 (2015)
779 132-143.
780 [73] J. Xiao, T. Yang, C. Wang, J. Xue, Y. Wang, Investigations on Radiation Tolerance of
781 Mn+1AXn Phases: Study of Ti3SiC2, Ti3AlC2, Cr2AlC, Cr2GeC, Ti2AlC, and Ti2AlN, J.
782 Am. Ceram. Soc., 98 (2015) 1323-1331.
783 [74] C. Ang, C. Silva, C. Shih, T. Koyanagi, Y. Katoh, S.J. Zinkle, Anisotropic swelling and
784 microcracking of neutron irradiated Ti3AlC2-Ti5Al2C3 materials, Scr. Mater., 114 (2016)
785 74-78.
786 [75] D.J. Tallman, L. He, B.L. Garcia-Diaz, E.N. Hoffman, G. Kohse, R.L. Sindelar, M.W.
787 Barsoum, Effect of neutron irradiation on defect evolution in Ti3SiC2 and Ti2AlC, J. Nucl.
788 Mater., 468 (2016) 194-206.
789 [76] C. Ang, S. Zinkle, C. Shih, C. Silva, N. Cetiner, Y. Katoh, Phase stability, swelling,
790 microstructure and strength of Ti3SiC2-TiC ceramics after low dose neutron irradiation, J.
791 Nucl. Mater., 483 (2017) 44-53.
792 [77] D.J. Tallman, L. He, J. Gan, E.a.N. Caspi, E.N. Hoffman, M.W. Barsoum, Effects of
793 neutron irradiation of Ti3SiC2 and Ti3AlC2 in the 121-1085 °C temperature range, J. Nucl.
794 Mater., 484 (2017) 120-134.

795

796

Figures captions

Fig. 1. Optical microscopy image of ZrCX-1.

Fig. 2. (a) Powder XRD patterns. Key: h, hexagonal Zr_2SC; and (b) Raman spectra of ZrCX-1, representative of ZrCX-1 to -3.

Fig. 3. (a) and (b) SEM images of ZrCX-1 and ZrCX-2 internal fractured surfaces at lower magnification, respectively; (c) and (d) SEM images of the same at higher magnification; (e) nitrogen adsorption-desorption isotherms; and (f) pore size distributions.

Fig. 4. Structural evolution of ZrCX-1 with temperature. (a) Powder XRD patterns. Key: t, tetragonal ZrO_2; h, hexagonal Zr_2SC; (b) micropore, external and BET surface areas; and (c) in-plane carbon crystallite size.

Fig. 5. Adsorption data. (a) Adsorption pH dependence for ReO_4^- adsorption onto ZrCX-1 and a carbon blank; (b) isotherm data for ReO_4^- adsorption onto ZrCX-1 at pH 5 with fitted Langmuir and Freundlich models.

Fig. 6. STEM studies of Re-loaded ZrCX-1. (a) Bright field image; and corresponding STEM-EDS elemental maps (b–e) of Zr, S, O and Re distributions.

33

819

820

821   Fig. 1. Optical microscopy image of ZrCX-1.

822

823
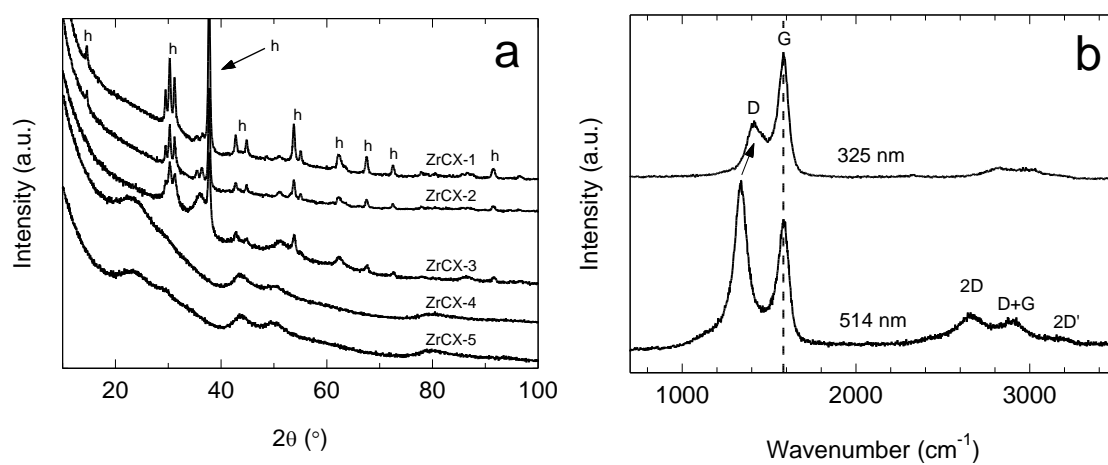
824

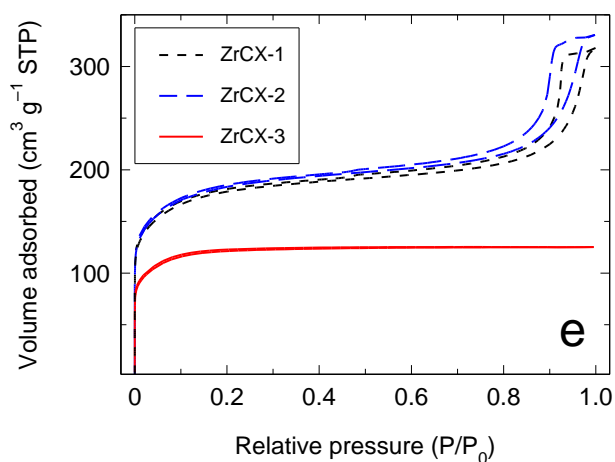825   Fig. 2. (a) Powder XRD patterns. Key: t, tetragonal ZrO_2; h, hexagonal Zr_2SC; and (b) Raman

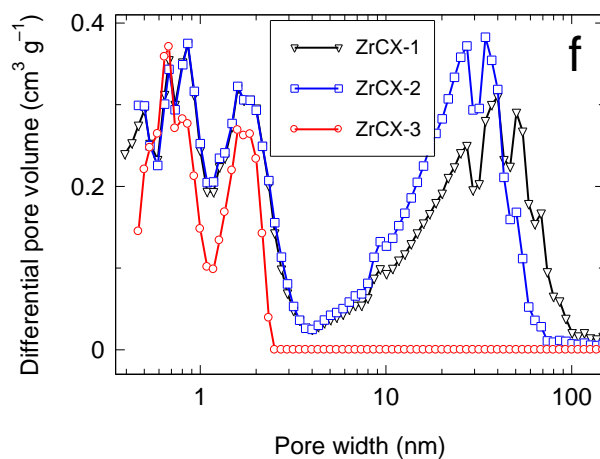826   spectra of ZrCX-1, representative of ZrCX-1 to -3.
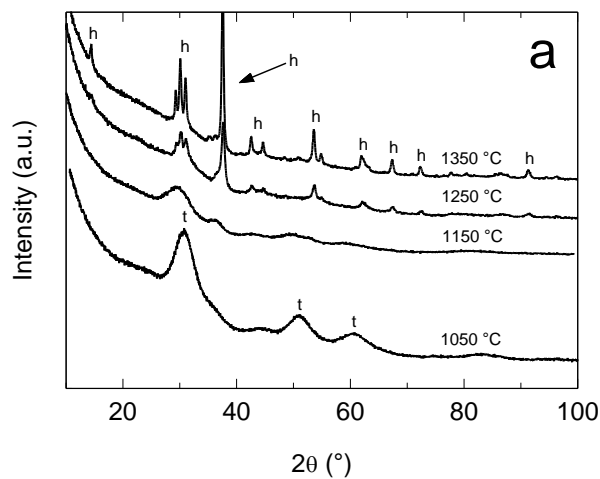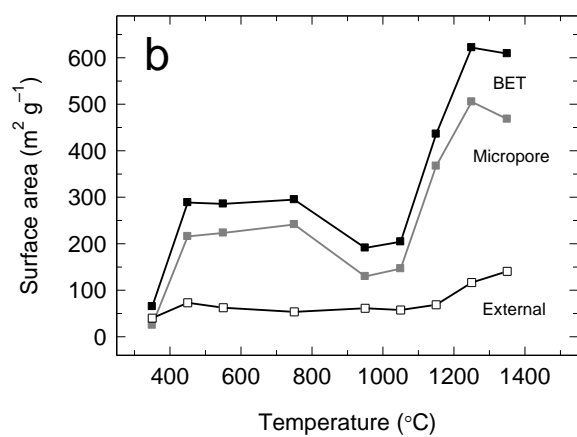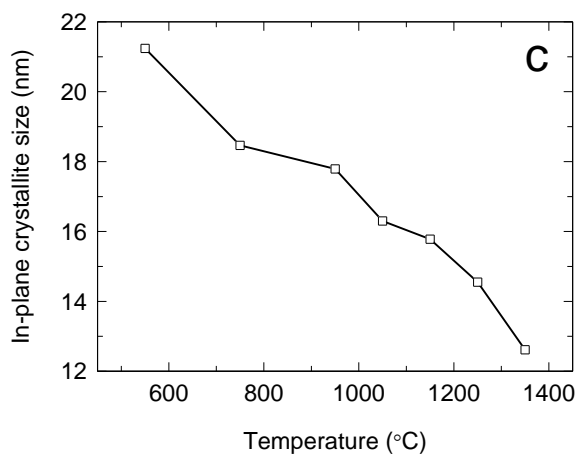
827

34

828
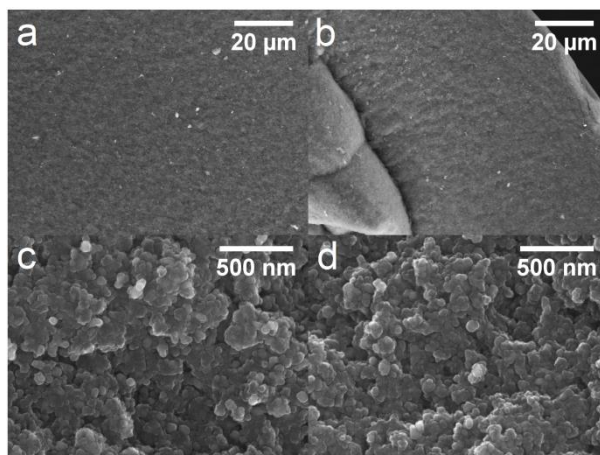
829

830

831   Fig. 3. (a) and (b) SEM images of ZrCX-1 and ZrCX-2 internal fractured surfaces at lower

832   magnification, respectively; (c) and (d) SEM images of the same at higher magnification; (e)

833   nitrogen adsorption-desorption isotherms; and (f) pore size distributions.
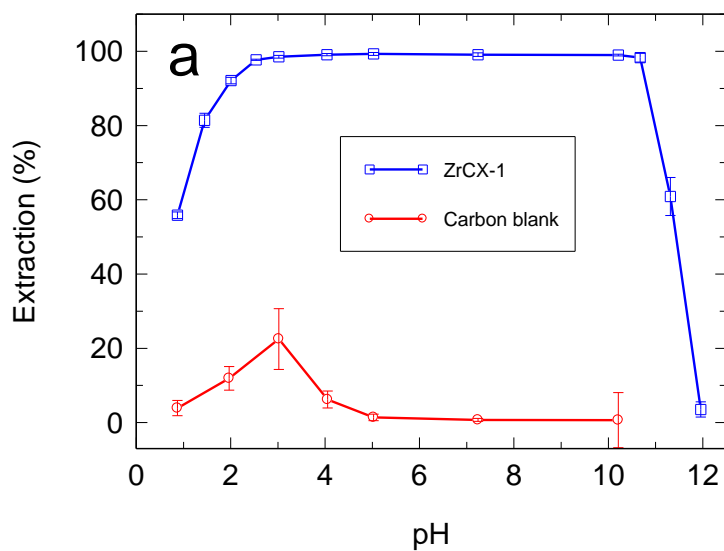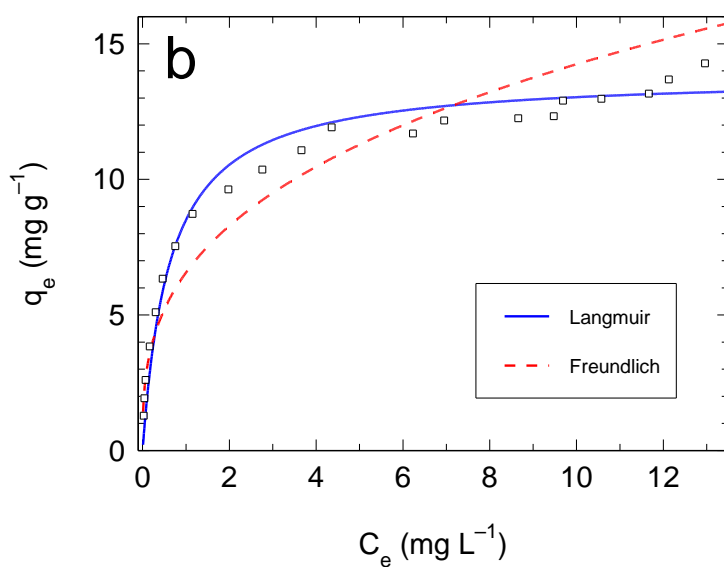
834

835

836

837   Fig. 4. Structural evolution of ZrCX-1 with temperature. (a) Powder XRD patterns. Key: t,

838   tetragonal ZrO_2; h, hexagonal Zr_2SC; (b) micropore, external and BET surface areas; and (c)

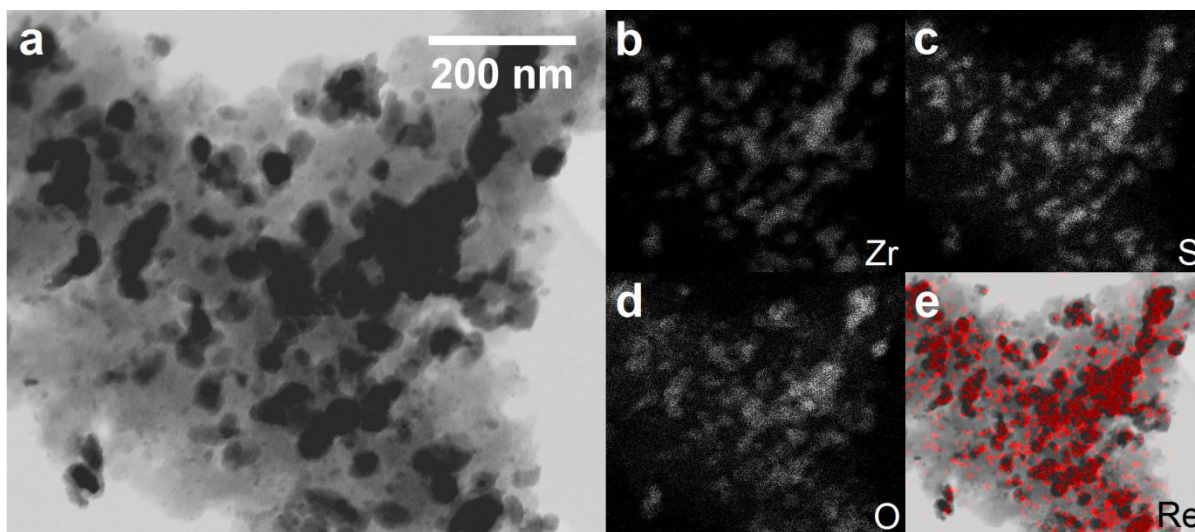839   in-plane carbon crystallite size.

840

841

842

Fig. 5. Adsorption data. (a) Adsorption pH dependence for ReO_4^- adsorption onto ZrCX-1

and a carbon blank; (b) isotherm data for ReO_4^- adsorption onto ZrCX-1 at pH 5 with fitted

Langmuir and Freundlich models.

846

847

848

849   Fig. 6. STEM studies of Re-loaded ZrCX-1. (a) Bright field image; and corresponding

850   STEM-EDS elemental maps (c–e) of Zr, S, O and Re distributions.

851

852